Earth Planet. Sci. Lett. 685 (2026) 120052

Contents lists available at ScienceDirect

Earth and Planetary Science Letters

journal homepage: www.elsevier.com/locate/epsl

A cautionary tale of disequilibria in microlite-melt evolution driven by fast crystallization kinetics: Implications for modeling volcanic processes

Jie Wu [a,b,1,*], Alessio Pontesilli [c,1,*], Marco Brenna [a], Shane J. Cronin [b], Sung-Hyun Park [d], Joali Paredes-Mariño [b], Kyle Hamilton [b,e], Marta Ribó [f], David Adams [b], Mila Huebsch [b]

[a] Department of Geology, University of Otago, Dunedin, 9054, New Zealand
[b] School of Environment, University of Auckland, Auckland, 1010, New Zealand
[c] Istituto Nazionale di Geofisica e Vulcanologia, Rome, 00143, Italy
[d] Korea Polar Research Institute, Incheon, 21990, Republic of Korea
[e] School of Earth & Atmospheric Sciences, Queensland University of Technology, Brisbane, 4001, Australia
[f] School of Science, Auckland University of Technology, Auckland 1010, New Zealand

ARTICLE INFO

Editor: Dr R. Hickey-Vargas

Keywords:
Magma evolution
Microlite crystallization
Crystallization kinetics
Volcanic bomb
Hunga eruption

ABSTRACT

An intact submarine-quenched bomb collected from the globally impactful 2022 Hunga eruption served as a natural laboratory to investigate the role of syn- and post-eruptive magma cooling on microlite crystallization and, in-turn, melt composition in mafic-intermediate magmatic systems. We investigated chemical-textural gradients across the bomb and elucidated the crystallization kinetics and cooling history via thermal modelling. High crystal growth rates correlate with increasing chemical and textural disequilibrium of clinopyroxene and plagioclase microlites towards the bomb interior. These reflect unsteady crystallization kinetics and especially a transition from dominantly interface-limited to diffusion-limited growth regimes. These far-from-equilibrium processes are cause for caution in applying constant experimentally-derived crystal growth rates to explain natural fast-cooling processes, potentially leading to inaccurate magmatic timescales. In this single bomb, far-from-equilibrium crystallization processes drove compositional trends that could be mistaken for pre-eruptive fractional crystallization. If not thoroughly assessed, such compositional effects may impair our ability to reconstruct crystal-melt equilibrium pairs and retrieve accurate thermobarometric estimates. Our results suggest that before examining magmatic reservoir processes in mafic-intermediate systems samples should be checked for the overprinting influences of syn- and post-eruptive crystallization, particularly if textural examination reveals high microlite numbers and extreme crystal morphologies.

1. Introduction

Rock textures, mineral abundances and morphologies along with whole-rock, mineral and glass compositions are fundamental to interpreting igneous and volcanic processes. These are typically interpreted within the context of well-established models of crystallization kinetics from which magma thermal histories are interpreted before solidification (Marsh, 1988; Cashman, 1993; Armienti, 2008). The timescales of crystallization and thermal evolution are calibrated against experimentally-derived kinetic models (Marsh, 1988; Pontesilli et al., 2019; Arzilli et al., 2022). In a closed system, crystallizing mineral phases directly control residual melt compositions. In stable magma reservoirs the system is not closed so that, near-equilibrium mineral fractionation occurs, with minerals lost due to gravitational settling (or left behind during filter pressing of a crystal mush during eruption); this drives bulk magma and melt evolution along liquid lines of descent. During and shortly after eruption, if chilling is not instantaneous, syn- and post-eruption decompression and cooling promote rapid crystal growth under non-equilibrium conditions that affect the residual melt chemistry (e.g., Hammer and Rutherford, 2002; Szramek et al., 2010). Hot magmas, especially those with mafic to intermediate compositions, reach increasingly far-from-equilibrium under high cooling rates, which

* Corresponding authors.
E-mail addresses: wujiext@gmail.com (J. Wu), alessio.pontesilli@ingv.it (A. Pontesilli).
[1] These authors contributed equally to this work.

https://doi.org/10.1016/j.epsl.2026.120052
Received 24 September 2025; Received in revised form 30 March 2026; Accepted 13 April 2026
Available online 20 April 2026

drives unexpected compositional contrasts on small spatial scales – such as within a single pyroclast (e.g., Falasconi et al., 2023).

Usually, magmatic processes are well reflected in rapidly cooled volcanic rocks, especially pyroclasts dispersed into plumes or pyroclastic density currents. Explosive eruptions produce tephra with a wide range of grain sizes from metre- to micron-scale. However, even the finest glassy ash particles (< 2 mm diameter) exhibit microlites during rapid cooling (Hunt and Hill, 1993). Also, if there is stalled or heterogeneous rates of magma ascent and multiple fragmentation episodes, highly variable crystallinity may result (e.g., Hammer et al., 1999; Colombier et al., 2018). To decipher pre-eruption from post-fragmentation textures and reconstruct crystallization histories is thus highly challenging. In this study we investigate how syn- and post-eruptive magma cooling may generate groundmass and microlite crystallization under spatially and temporally varying crystal growth regimes and thus modifies melt compositions in unexpected ways. Recognising these complex processes is important when using glass chemistry to interpret the thermobarometry of pre-eruptive magma storage/decompression, timescales of magma residence and magma ascent rates, as well as understanding eruptive sources of unknown pyroclastic units (Hunt and Hill, 1993; Hammer and Rutherford, 2002; Putirka, 2008; Lormand et al., 2020; Hutchison et al., 2025). For example, microlite crystallization in Fagradalsfjall magma resulted in underestimation of calculated magma temperature by modifying melt compositions (Hafsteinsdóttir, 2024). Similarly, assuming a particular, experimentally-derived growth rate for the whole crystal population in crystal size distribution-based studies may indeed affect the calculated timescale more than the microstructure itself (Brugger and Hammer, 2010; Cashman, 2020). Here we investigated the complexities of far-from equilibrium crystallisation using a submarine-quenched volcanic bomb from the explosive 15 January 2022 Hunga eruption of Tonga. Volcanic bombs (i.e., >64 mm in diameter) are an ideal natural laboratory for investigating far-from-equilibrium crystallization processes, because the different cooling rates from bomb rim to interior lead to the development of a wide range in crystallinity. This natural sample, due to the progressive development of post-fragmentation crystallinity in a closed system where thermal histories may be independently constrained, allows for a direct comparison of kinetic parameters with experimental-based studies, allowing the linking of natural crystallization processes to laboratory observations. By contrast, piecing data together from smaller pyroclasts, such as ash fragments <2 mm, means that assumptions need to be made about how individual particles relate to each other and the spatio-temporal variability of the magma, especially during a large complex eruption lasting several hours. The ash particles thus include a wider range of less-controlled variables and may also include pre-fragmentation crystallization within a dyke system (e.g., Cashman, 1993). The advantage of a bomb sample is that it captures the entire cooling history from a single conformable sample of microlite-free magma that provides closed system constraints to draw comparisons with experimental results.

Located in the Tonga-Kermadec island arc in the South Pacific Ocean, Hunga is a mostly submarine volcano characterized by a ~4 km-diameter caldera (Fig. 1a; Brenna et al., 2022; Le Mével et al., 2023). Recent Surtseyan style eruptive activity in 2009 and 2014–2015 lasted months, building emergent tuff cones. The latest eruption started on 19 December 2021, with sustained Surtseyan activity producing low ash-poor plumes, culminating in an 11-hour long, climactic volcanic explosivity index (VEI) 6 eruption on 15 January 2022 (Gupta et al., 2022). The eruption ejected at least 6–10 cubic kilometers of pyroclastic deposits (Clare et al., 2023) forming tephra and submarine mass flow deposits and extremely large tsunami (Borrero et al., 2023). The eruption produced a 500-km-radius, ~30 km-high umbrella cloud, with an overshoot portion extending into the mesosphere at 58 km-high (Proud et al., 2022).

Ash and lapilli from the entire Hunga eruptive sequence show a large range of microlite contents and have a glass compositional range from andesite to dacite (Wu et al., 2025, Wu et al., 2026). This compositional and textural diversity is replicated within single intact volcanic bombs

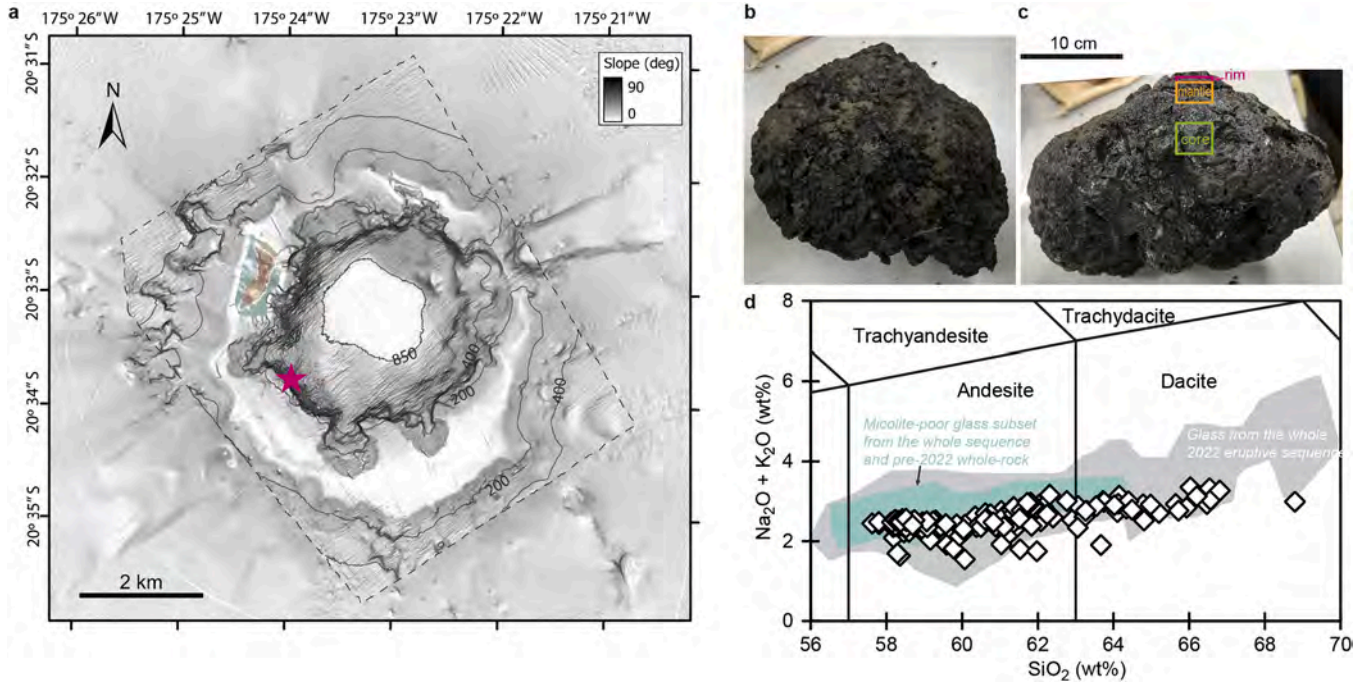

Fig. 1. Map of Hunga volcano and 2022 volcanic bomb texture and composition. (**a**) Slope gradient map of the Hunga volcano caldera, with contour lines indicating the water depth and pink star showing the sample location. (**b**) Hand specimen of the 2022 Hunga bomb viewed from the top showing the intact rim surface. (**c**) Cross-section-view of the bomb with the sampled core, mantle, and rim regions marked. (**d**)Total alkali silica (TAS) diagram showing the Hunga bomb glass composition; glass composition from the whole 2022 eruptive sequence regardless of microlite contents (turquoise shaded area), and a subset of microlite-poor glass data from the whole sequence, along with pre-2022 Hunga whole-rock compositions (grey shaded area; Brenna et al., 2022; Wu et al., 2025,2026) are shown for comparison.

erupted below sea-level. This implies that the post-fragmentation cooling in the bomb mimics the syn-fragmentation processes within the conduit. Thus, the fast crystallization kinetics and the effect on post-fragmentation melt evolution reconstructed on the basis of the bomb groundmass, can also be applied to syn-eruptive conduit processes. Indeed, rapid crystallization kinetics are also documented in rapidly chilled dyke margin (e.g., Cashman, 1993; Chistyakova and Latypov, 2010). The glass compositional gradients inside the bombs correlate with changes in microlite texture, composition and abundance from microlite-poor glassy rims to almost fully crystalline interiors. Similar trends between microlite crystallization and glass composition were identified in studies at other volcanoes (e.g., Hammer et al., 1999; Falasconi et al., 2023), although these were interpreted across several individual pyroclastic particles and over a narrower range of crystallinity than seen at Hunga. The zoned bomb we studied allows for a wide range of textures, allowing a broad investigation of how subtle differences in post-eruptive cooling history generates major changes in groundmass crystal populations, including crystal size distribution (CSD) and chemical properties. Thus, this natural sample enables us to bridge the gap between experimental results and natural crystallization processes and especially highlight far-from-equilibrium crystallization processes in a way that is not afforded by lapilli or ash particles with uncertain relationships to each other in the spatial-temporal context of a large magma body.

2. Samples and methods

2.1. Sample information

The sample examined (DG03-C) was one of several bombs dredged from the inner caldera wall in the southern sector of the volcano at a depth of >300–500 m below sea-level, during a survey conducted onboard of the RV Aaron (Korea Polar Research Institute) in April 2022 (Fig. 1). The bomb was selected as one of five similar pyroclasts, all with distinctive macroscopic changes in texture from surface to core. Samples taken from the core, mantle, and rim of DG03-C were made into three polished epoxy mounts for textural and compositional analyses using electron microprobe analysis (EMPA) at University of Auckland (see supplementary methods in Appendix A). EMPA data for glass, plagioclase, pyroxene and standards are all available in Tables S1 to S3 in Appendix B.

2.2. Textural analysis and crystal size distribution

Back-scattered electron (BSE) images for microlite textural analysis (Fig. S1) have magnifications from 130× to 850×, with a total phenocryst- and vesicle-free matrix area of 0.7 (bomb rim), 0.5 (mantle) and 2.4 (core) mm^2. The ImageJ software package was used for image processing (i.e., thresholding and segmentation) and textural analyses (crystal counting and size measurements; see Table S4), following Brugger and Hammer (2010) and Pontesilli et al. (2019). Boundaries between touching crystals were identified through visual inspection of crystal morphologies, which reduced potential error introduced by the probability of multiple intersections of concave crystal shapes in the analytical plane. The uncertainty of this method is likely negligible due to the large number of crystals examined; 778, 4399 and 3948 for plagioclase and 6830, 8873 and 14257 for clinopyroxene, in the bomb rim, mantle and core, respectively. As detailed in Pontesilli et al. (2019), to reduce the error introduced in the segmentation process, we estimated the crystal fraction uncertainty as the change in measured crystal area determined by the addition and subtraction of a pixel layer around each crystal in the binary image, and the relative error is <10% of the measured total crystal area.

CSD analyses are performed only on microlites, following Armienti (2008) and Higgins (2000), with the stereological correction (2D to 3D) carried out via the "unfolding" method based on the algorithms introduced by Saltykov (1949) and Schwartz (1939). CSD calculations are performed via the CSDCorrections software (Higgins, 2000), adopting linear size bins as suggested by Armienti (2008). 3D aspect ratios are estimated from the 2D aspect ratios of the crystal populations following Mangler et al. (2022). To ensure the most accurate CSD is chosen for each crystal population, binning was based on the minimization of the number of particles (zeroth moment of the distribution; Eq. (1)) and the total crystal volume (third moment of the distribution; Eq. (2)) between the measured 2D populations and the corrected 3D populations used in CSD analyses:

$$N_{tot} = Area\sum_i L_i N_V(L_i) \tag{1}$$

$$V_f = \sum_i N_V(L_i)V_i = \sigma\sum_i L_i^3 N_V(L_i) \tag{2}$$

Where the shape factor σ is determined by:

$$\sigma = \left[1 - \Omega\left(1 - \frac{\pi}{6}\right)\right]\frac{IS}{L^2} \tag{3}$$

Where L is the maximum crystal length measured in 2D, L_i the midpoint length of the i^{th} size bin and $N_V(L_i)$ its volume number density, Ω the average roundness of the crystal population, and *S, I, L* the short, intermediate and long dimension of the 3D crystal shape, respectively (Higgins, 2000).

The CSD data are plotted as the natural logarithm of $N_V(L_i)$ vs L_i. To avoid any bias in the determination of crystal sizes approaching resolution limits, CSD calculated considering all crystal intersections measured in plane are compared to CSD calculated after filtering for crystals smaller than 1 μm^2 (sampled by 9 pixels at the lowest magnification). No appreciable difference is observed between filtered and unfiltered CSD, testifying to the accuracy of our crystal segmentation strategy.

Crystallization kinetics are then described using existing classic formulations. Maximum apparent growth rates (G_{max}) are estimated considering the average crystal size of the 1% largest crystals measured in 2D:

$$G_{max} = \frac{(lw)^{0.5}}{2t} \tag{4}$$

Where l and w represent the length and width of the crystal intersection, respectively, and the factor 2 refers to the growth of half-crystal during advancement of the pinacoid face (Pontesilli et al., 2019; Brugger and Hammer, 2010). Time for each sample collected across the bomb radius (core, mantle and rim) corresponds to the cooling time estimated by thermal modeling (Table 1). Accordingly, growth and nucleation rates are apparent, since crystallization kinetics are treated as constant during the cooling process. Nucleation (J) and growth rates for whole crystal populations can be calculated from CSD plots, following Marsh (1988) and Randolph and Larson (1988):

$$Slope_{CSD} = -\frac{1}{L_d} = -\frac{1}{2\ Gt} \tag{5}$$

$$J = N_0 G \tag{6}$$

Where L_d is the characteristic crystal size representing the ratio between the total length and the total number of crystals (Cashman, 1992; Marsh, 1998; Pontesilli et al., 2019), and N_0 is the density of crystal nuclei, which is the intercept value of the CSD plot and represents the extrapolation of crystal number density at zero crystal size (Marsh, 1988). Accordingly, J calculated from CSD plots represents the nucleation rate expressed by the final population of nuclei when the cooling curve crosses the glass transition temperature (T_g).

Table 1
Microlite textural data and thermal modeling parameters for the 2022 Hunga volcanic bomb.

Sample	Bomb core		Bomb mantle		Bomb rim	
Crystal population	Plagioclase	Clinopyroxene	Plagioclase	Clinopyroxene	Plagioclase	Clinopyroxene
Microlite area (%)	25.3	18.8	21.7	25.8	2.4	4.4
Microlite N_A (mm^{-2})	5284	9730	9080	18334	320	6146
CSD slope	−81.7	−91.1	−80.7	−93.6	−99.4	−108.7
CSD intercept	17	17.4	17.4	17.1	14.6	16.2
Maximum crystal size (mm)*	0.013	0.0096	0.0095	0.0096	0.0098	0.0062
d_{CSD} (mm)	0.0061	0.0055	0.0062	0.0053	0.0050	0.0046
3D aspect ratio	1:3.5:6	1:1.5:4	1:4.1:6.8	1:1.5:4.6	1:5:6.8	1:1.1:4.2
T_g (K)	802		798		814	
Cooling time (s)	2900† / 3960‡		1800† / 2630‡		340† / 490‡	
Average cooling rate ($K\ s^{-1}$)	0.19† / 0.12‡		0.32† / 0.21‡		2.32† / 1.69‡	
G_{max} (x 10^{-6} mm s^{-1})#	3.34–4.57	2.44–3.34	3.60–5.27	3.64–5.33	19.9–28.7	12.7–18.2
G_{CSD} (x 10^{-6} mm s^{-1})#	1.54–2.11	1.38–1.89	2.35–3.44	2.03–2.97	10.3–14.8	9.39–13.5
J ($mm^{-3}\ s^{-1}$)#	20.9–28.5	27.9–38.1	44.9–65.6	29.6–43.2	21.9–31.5	98.8–142.4
Av#	0.22–0.30	0.28–0.38	0.13–0.19	0.14–0.20	0.04–0.05	0.06–0.09

* Maximum crystal size calculated as the average of the 1% largest crystals in each population.
† Results for latent heat (LH)-free thermal model.
‡ Results for model including LH.
# Minimum and maximum values for estimated crystallization kinetics were calculated considering the thermal models with and without the LH-effect, respectively.
Note that microlite area proportion is an average of each sample for the bomb core, mantle, and rim.

2.3. Thermal modeling

To model the thermal evolution of the volcanic bomb after magma fragmentation, the one-dimensional heat equation is solved in spherical coordinates (Bergman, 2011):

$$\rho_m C_p \frac{\partial T}{\partial t} = \frac{1}{r^2}\frac{\partial}{\partial r}\left(kr^2\frac{\partial T}{\partial r}\right) \quad (7)$$

Where the independent spatial variable r is the bomb radius, and ρ_m the density of the Hunga andesitic magma (2650 kg m^{-3}; Wu et al., 2025). The temperature- and compositional-dependent heat capacity (C_p; J $kg^{-1}\ K^{-1}$) and thermal diffusivity (a; $m^2\ s^{-1}$) are estimated through the calibrations of Hofmeister et al. (2016) and Stebbins et al. (1984), considering the andesitic bulk composition of the Hunga magma. These parameters also allow calculation of the temperature-dependent thermal conductivity (k; W $m^{-1}\ K^{-1}$):

$$k = \rho_m C_p a \quad (8)$$

Eq. (7) is solved using the partial differential equation solver in MATLAB that discretizes the heat equation following Skeel and Berzins (1990). To account for the effect of latent heat released by the groundmass crystallization inside the bomb, we also implemented a source term assuming a linear increase in crystallization from 0% at the bomb surface to 50% at 30 mm-distance from the same bomb surface (see below). Although a thorough assessment of latent heat is beyond the scope of this work as it requires knowing a priori the temporal evolution of crystallization kinetics, this simplified approach allows us to define an upper limit to the total groundmass crystallization time (t_c) estimated, taken as the time needed for the different zones of the bomb to cool down to T_g.

During the 2022 Hunga eruption, magma fragmentation mainly occurred at depth of 400–1000 m below sea-level (Wu et al., 2025), which suggests the bomb most likely cooled underwater. Thus, the right-hand boundary condition, where interaction between the bomb surface and water occurs, was set by a combination of convective and radiative heat flux at the sample-water interface, after Moitra et al. (2018, 2020):

$$\frac{\partial T}{\partial r} = \frac{1}{k}\left[h_c\left(T_{surf} - T_{sat}\right) + \varepsilon S_B\left(T_{surf}^4 - T_{sat}^4\right)\right] \quad (9)$$

Where ε represents the emissivity, exhibiting limited variability for silicate melts (0.97–0.99, adimensional; Ball and Pinkerton, 2006) and set at 0.97. S_B is the Stefan-Boltzmann constant (Bergman, 2011), and h_c the convective heat transfer coefficient, taken as a constant of 4000 $W\ m^{-2}\ K^{-1}$ following Moitra et al. (2020). T_{surf} represents the temperature at the bomb surface and T_{sat} the temperature at which water is saturated with vapor. T_{sat} is set at 150 °C to account for the increase in water boiling temperature with pressure in the depth of 200–1000 m (Lide, 2004), according to bathymetric surveys of the caldera top before and after the eruption (Cronin et al., 2017; Ribo et al., 2023). The left-hand boundary condition, at the bomb center, is fixed by the spherical symmetry:

$$\frac{\partial T}{\partial r} = 0;\ r = 0;\ t \geq 0 \quad (10)$$

While the initial condition is set considering an eruptive temperature (T_i) of 1050 °C (after Brenna et al., 2022) at time zero. To evaluate the temporal interval relevant to crystallization of the initially glassy groundmass, T_g is estimated by the Artificial Neural Network model trained by Langhammer et al. (2022), considering the average glass composition for each portion of the Hunga bomb and a melt water content of 1.7 wt% based on average groundmass glass Raman measurements on the outer bomb (Wu et al., 2025). Total crystallization time is taken again as t_c, the cooling time from T_i to T_g for each sampled portion of the bomb. Average cooling rate is then calculated as $T_i - T_g$ divided by t_c.

3. Results

3.1. Textural gradient

The 2022 Hunga volcanic bomb has a flattened-ovoid shape with a glass encrusted surface (possibly the top of the sample; Fig. 1b) and an apparent area of abrasion on the other side (Fig. 1c). It measures on average ~10 cm in radius (longest axis 26 cm, shortest 16 cm). The bomb was sub-sampled to capture the contrasts in texture seen in hand specimen at three positions: core, at 50–70 mm from the rim (at ~50 mm radius from the center); mantle, at ~10–30 mm from the rim (70 mm radius); and rim, the outermost 5–10 mm (90 mm radius) (Fig. 1c).

The bomb is composed of glass, plagioclase, and pyroxene (Fig. 2). Average vesicle proportions increase from the bomb rim (15 vol%) to the mantle and core (27–34 vol%). Crystals are dominantly microlites, with length typically <100 μm. Their average volume (area) fraction (excluding vesicle and phenocryst) increases from 7 vol% for the entire bomb rim (5–10 mm from the bomb surface) to overall 44–48 vol% in

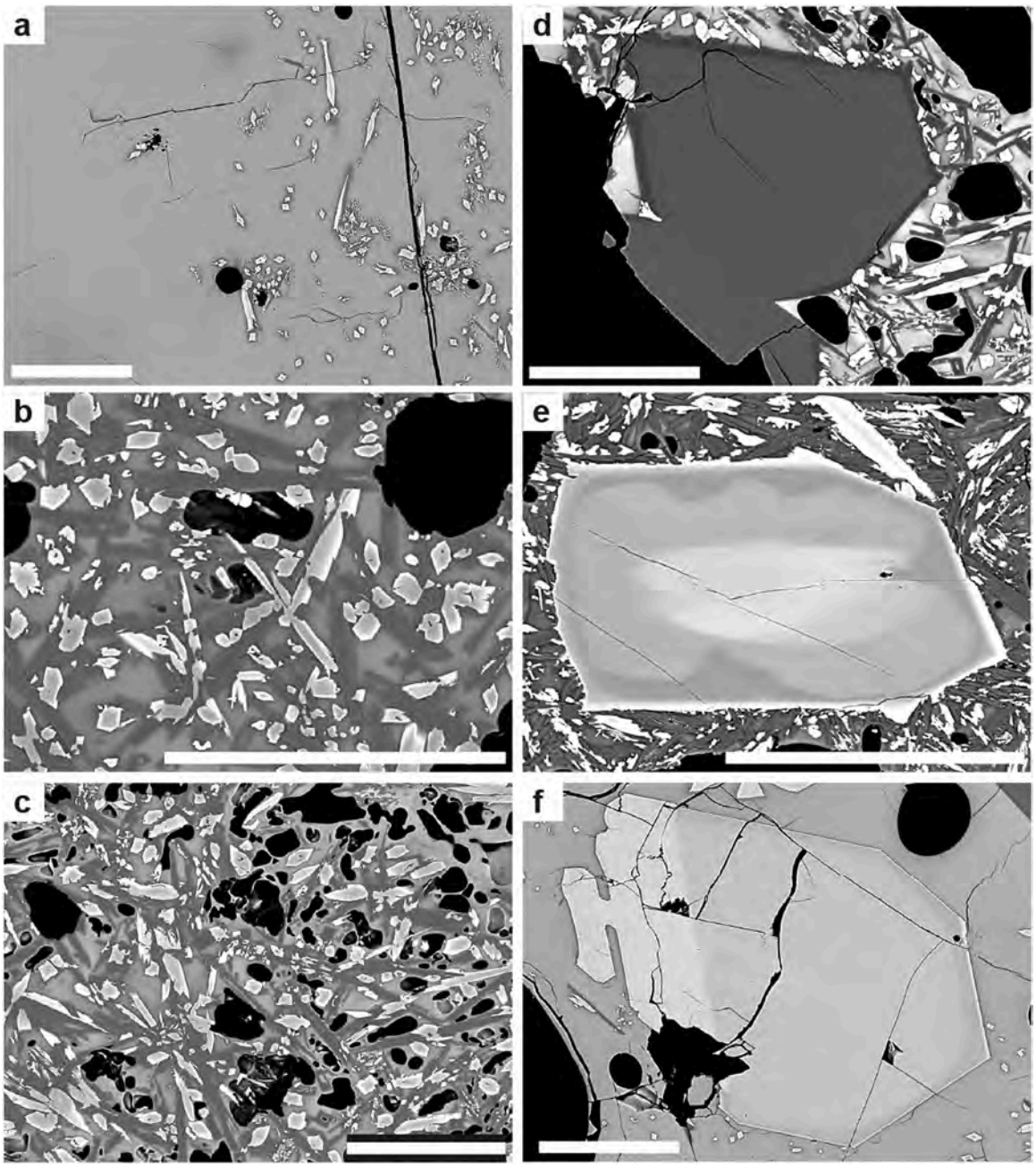

Fig. 2. Back-scattered electron (BSE) images showing the texture of matrix glass and mineral phases from the 2022 Hunga bomb. (**a**) Transition of microlite-free to microlite-poor glass from left to right in the bomb rim. (**b**) Microlite-rich matrix glass from the bomb mantle. (**c**) Microlite-rich matrix glass from the bomb core. (**d**) A homogenous plagioclase core rimmed by a thin Ca-poor overgrowth. (**e**) Reversely zoned orthopyroxene with a thin overgrowth of pigeonite (bright rim). (**f**) Coexisting of reversely zoned orthopyroxene (right) and homogenous clinopyroxene (left, bright). Scale bar represents 100 μm. In matrix, the brightest and darkest phases are clinopyroxene and plagioclase respectively, and the phase with intermediate brightness is glass.

the interior (mantle + core; ~30–50 mm from the bomb surface) (Figs. 2a–c and 3a). Microlites consist exclusively of plagioclase and clinopyroxene. As crystallinity increases, plagioclase microlites become volumetrically dominant over clinopyroxene. From the bomb rim to interior, plagioclase-to-clinopyroxene microlite volume ratio increases from 0.5 to 1.3, also reflected by an increase in their number density (N_A) for both plagioclase (320 to 5284–9080 mm^{-2}) and clinopyroxene (6146 to 9730–18334 mm^{-2}) (Fig. 3b; Table 1). Rare plagioclase microlites occur at the bomb rim, characterized by mostly subhedral to euhedral morphologies (Fig. 2a). Skeletal (hopper) morphologies characterize the more abundant plagioclase microlites in the bomb interior (Fig. 2b and c). Likewise, clinopyroxene microlites have acicular shapes in the bomb rim, whereas subhedral to dendritic crystals are observed in the bomb interior (Fig. 2b and c).

Average 2D aspect ratios for plagioclase are 4 ± 3 (bomb core; average and interquartile range values), 4.5 ± 3.2 (mantle) and 5.6 ± 5.2 (rim) best fitted by average 3D crystal shapes of 1:3.5:6 (bomb core), 1:4.1:6.8 (mantle) and 1:5:6.8 (rim). Clinopyroxene microlites have lower bidimensional aspect ratios, equal to 2.2 ± 1.2 (bomb core), 2.2 ± 1.3 (mantle) and 2.1 ± 1.2 (rim), for which the best fit 3D aspect ratios are 1:1.5:4 (bomb core), 1:1.5:4.6 (mantle) and 1:1.1:4.2 (rim). The CSDs for plagioclase microlites are linear and mostly parallel at crystal sizes <105 μm, although those from the bomb mantle have slightly steeper slope (Fig. 3c and Table 1). Notably, while plagioclase

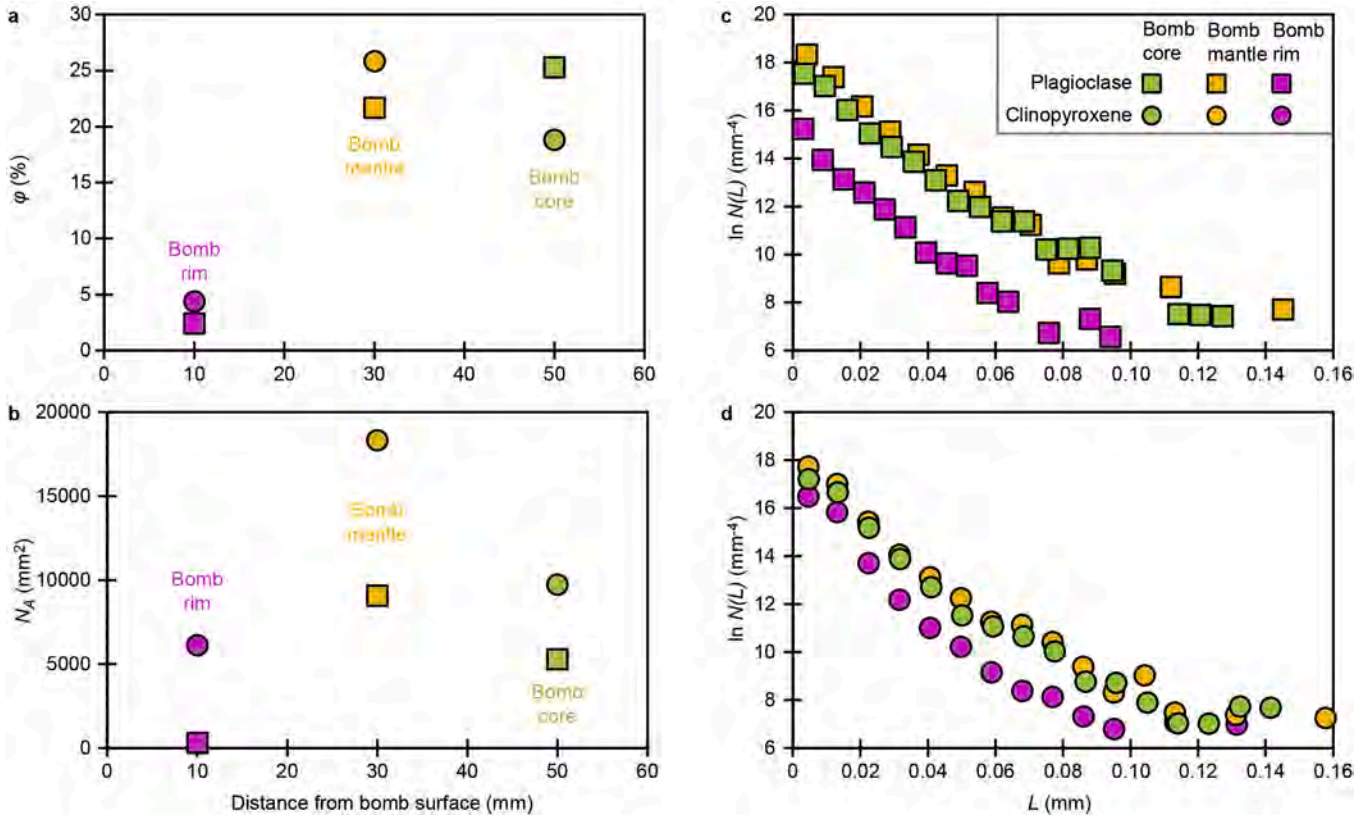

Fig. 3. Main textural parameters for microlites from the 2022 Hunga bomb. (**a**) Area fraction (φ) for plagioclase and clinopyroxene. (**b**) Number density (N_A) for plagioclase and clinopyroxene. (**c**) Plagioclase crystal size distribution. (**d**) Clinopyroxene crystal size distribution.

populations from the bomb mantle and core almost overlap, the rim sample displays a lower intercept value which reflects the lower crystal abundance towards the glassy carapace of the bomb (Fig. 2a). CSDs for clinopyroxene microlites are also mostly linear below 70 μm, or with slightly concave upward trends (Fig. 3d and Table 1). The population in the bomb rim has lower values across all size bins, in agreement with the lower crystal abundance (Table 1).

Phenocrysts and microphenocrysts (typically ≥100 μm) represent a minor fraction of the bomb volume, typically <10 vol%, without significant variability across the entire bomb. Phenocrystic plagioclase is normally zoned with a <10-μm-thick rim compositionally similar to microlites (Fig. 2d). Orthopyroxene and clinopyroxene are the dominant phenocryst phases and show alternatively normal or reverse zoning, with a compositionally distinct <10-μm-thick rim (Fig. 2e and f).

3.2. Mineral composition

Phenocrystic plagioclase cores are Ca-rich with An# (= molar Ca/(Ca + Na + K) × 100) mostly between 84 and 95 (Fig. 4a). Rims are compositionally similar to microlites; both are distinctively more evolved (An_{67-82}). FeO, MgO and TiO_2 in plagioclase are negatively correlated to An#. Compared to plagioclase cores, rims and microlites have distinctly higher FeO (0.87–2.62 vs 0.50–0.99 wt%), MgO (0.21–1.26 vs 0.08–0.21 wt%), and TiO_2 (0.02–0.17 wt% vs majority below detection limit) (Figs. 4b and S2).

Spatially across the bomb, the compositional ranges of phenocrystic plagioclase cores are invariant. Rim and microlite compositions, however, extend to more evolved compositions in the bomb interior, relative to the bomb rim, including lower An# (An_{67-80} vs An_{72-82}) as well as higher FeO (0.87–2.62 vs 0.88–1.82 wt%), MgO (0.24–1.26 vs 0.21–0.66 wt%), and TiO_2 (0.02–0.17 vs 0.02–0.08 wt%) (Figs. 4a, b and S2).

Phenocrystic pyroxene interior (core and mantle) compositions are enstatite ($En_{65-81}Fs_{15-30}Wo_{3-5}$, i.e., Enstatite, Ferrosilite and Wollastonite) and augite ($En_{44-50}Fs_{8-19}Wo_{32-42}$) (Fig. S3a). Rim and microlite are augite and pigeonite ($En_{28-69}Fs_{21-49}Wo_{5-39}$). Here, the "rim" refers to the outermost thin (few microns or less thickness) overgrowth on both clinopyroxene and orthopyroxene phenocrysts, which resembles microlite composition (Figs. 2f and 4). Compared to phenocrystic clinopyroxene interior, rim and microlite have much larger compositional variations, with distinctively lower Mg# (= molar Mg/(Mg + Fe) × 100, 36–73 vs 72–86; Fig. S3b), and higher Al_2O_3 (2.01–11.03 vs 1.53–2.82 wt%) and TiO_2 (0.14–0.89 vs 0.10–0.29 wt% (Fig. 4c). Clinopyroxene formula and components were calculated following Putirka (2008) and Petrone et al. (2022). In both phenocryst and microlite, ^{T}Si is correlated positively with ^{M1}Mg, and negatively with ^{T}Al, ^{M1}Al, and $^{M1}Fe^{tot}$. All clinopyroxene compositions align along a continuous negative-slopped array in $^{IV}Al + {}^{VI}Al + {}^{M1}Ti + {}^{M1}Fe^{tot}$ vs $^{T}Si + {}^{M1}Mg$ plot (Fig. 4d), with phenocryst interior sitting at the highest $^{T}Si + {}^{M1}Mg$ end. This suggests that enrichment in Al and Ti is a result of enhanced Tschermak (Ts = CaTs + CaTiTs + CaFeTs) substitution; ^{T}Al substituting ^{T}Si at tetrahedral site, is coupled with replacement of ^{M1}Mg by ^{M1}Al, ^{M1}Ti, $^{M1}Fe^{tot}$ at M1 site.

Spatially across the bomb, pyroxene rim and microlite compositions from the bomb interior have slightly lower overall Mg# (mode at 67 vs 71; Fig. S3b) and show larger scatters in Al_2O_3 and TiO_2 at a given Mg#, compared to those in the bomb rim.

3.3. Glass composition

Glass from the 2022 Hunga bomb is andesite to dacite in composition (Figs. 1d and 5). Overall, the glass spans a large compositional range in all major elements including SiO_2 (57.80–68.79 wt%), Al_2O_3 (12.18–16.10 wt%), Na_2O (1.02–2.41 wt%), K_2O (0.36–1.14 wt%), CaO

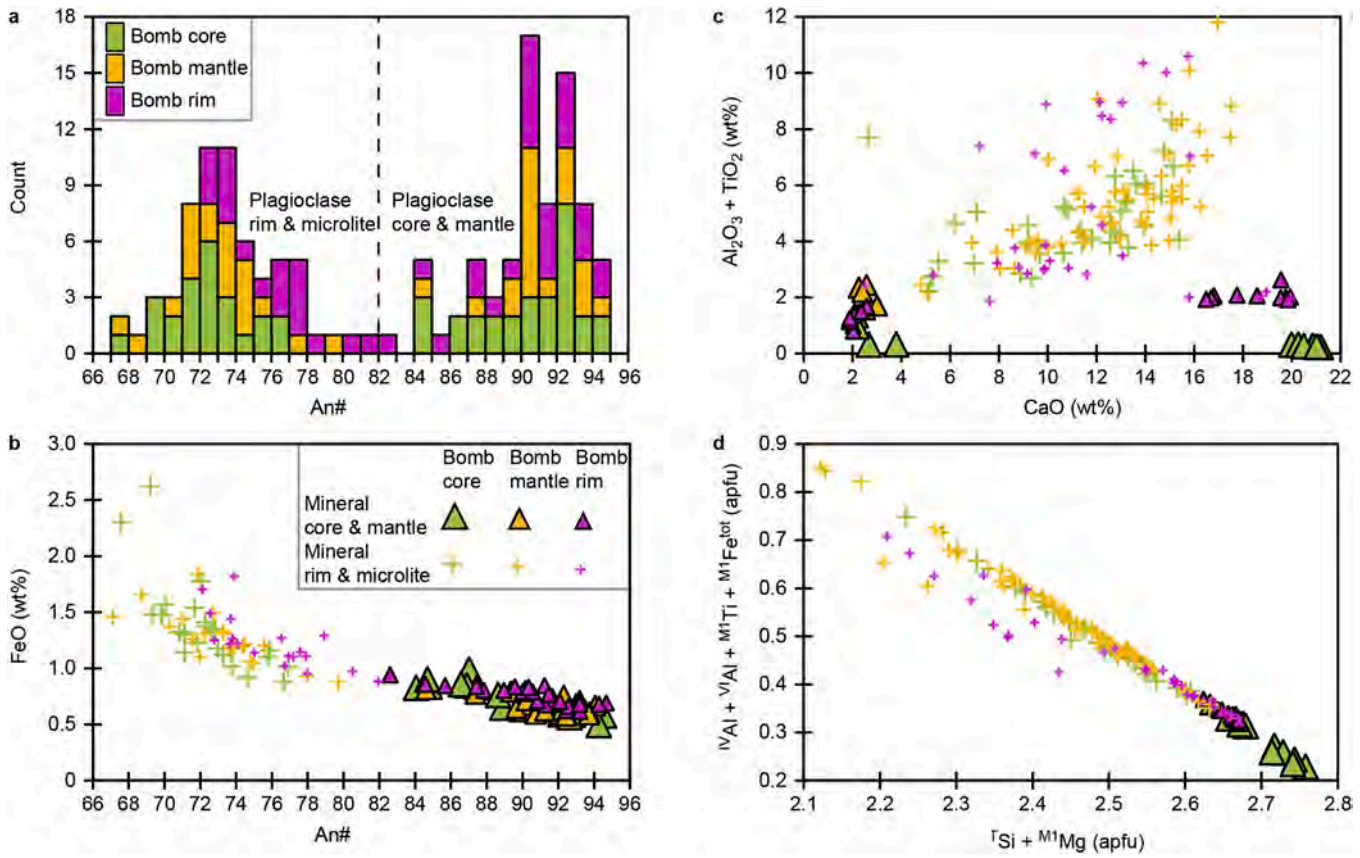

Fig. 4. Compositions of microlites and phenocrysts from the 2022 Hunga bomb. (**a**) Histogram showing An# (= molar Ca/(Ca + Na + K) × 100) distribution in plagioclase. (**b**) FeO vs An# in plagioclase. (**c**) $Al_2O_3 + TiO_2$ vs CaO in both clinopyroxene and orthopyroxene. (**d**) $^{IV}Al + {}^{VI}Al + {}^{M1}Ti + {}^{M1}Fe^{tot}$ vs $^{T}Si + {}^{M1}Mg$ in clinopyroxene.

(5.28–9.20 wt%), TiO_2 (0.57–1.16 wt%), MgO (0.27–5.57 wt%), FeO (7.31–13.39 wt%), and P_2O_5 (0.06–0.20 wt%) (Figs. 5 and S4). The Mg# ranges from 6 to 47 (Fig. S4). SiO_2 correlates positively with K_2O, and negatively with CaO, MgO, TiO_2, and Mg# (Figs. 5 and S4).

Spatially across the bomb, the rim glass is the most homogenous (e.g., 57.80–60.47 wt% SiO_2). Glasses from the bomb mantle and core have similar large compositional variations (58.98–68.79 and 57.81–66.47 wt% SiO_2, respectively), but at low SiO_2, they both have lower Al_2O_3 and higher FeO and TiO_2 than rim glass.

3.4. Bomb crystallization and thermal evolution

Based on temperature-time evolution curves calculated using two thermal models including and excluding latent heat respectively for the Hunga bomb (see details in Section 2.3), the total crystallization times are 340–490, 1800–2630 and 2900–3960 s, respectively for the bomb rim, mantle, and core (Table 1; Figs. 6a and S5). Crystal growth rates determined by the two methodologies described above retrieve only slightly but systematically higher crystal growth rates for plagioclase ($G_{CSD} = 1.5–15 \times 10^{-6}$ mm s^{-1}; $G_{max} = 3.3–29 \times 10^{-6}$ mm s^{-1}) than for clinopyroxene ($G_{CSD} = 1.4–14 \times 10^{-6}$ mm s^{-1}; $G_{max} = 2.4–18 \times 10^{-6}$mm s^{-1}), also expressed by the subtle differences in microlite characteristic crystal sizes (d_{CSD}, Table 1). Such growth rates are in good agreement with the fast crystallization kinetics estimated for these phases from crystallization experiments under high degrees of undercooling and high cooling/decompression rates (Pupier et al., 2008; Brugger and Hammer, 2010; Arzilli et al., 2015; Pontesilli et al., 2019; Le Gall et al., 2021), where crystal textures are typically interpreted as the result of growth under far-from-equilibrium conditions (e.g., dendritic and skeletal crystals).

Due to increasing crystallization time, calculated crystal growth rates for both plagioclase and clinopyroxene decrease from the bomb rim to core (Figs. 7 and S6). Thus, the natural logarithms of growth rate show perfect linear correlation with those of both crystallization time (inversely) and cooling rate (positively), similar to reported relations in both natural and experimental case studies (e.g., Cashman, 1993; Pontesilli et al., 2019).

From CSD plots, nucleation rates are generally lower for plagioclase compared to clinopyroxene (21–66 vs 28–142 mm^{-3} s^{-1}). Comparable results are reported in the experimental literature at moderate-high undercooling and few hours of crystallization time (Arzilli et al., 2015), as well as in dikes crystallized at high cooling rates (Cashman, 1993). In contrast to growth rates, nucleation rates do not exhibit linear relationships with crystallization time or equivalently, with cooling rate (Fig. 7).

4. Discussion

4.1. Microlite evolution during post-fragmentation crystallization

Microlite crystallization can result from decompression-induced volatile loss during magma ascent, thus microlites from tephra are often used to estimate decompression rates (Hammer and Rutherford, 2002; Brugger and Hammer, 2010). However, post-fragmentation microlite crystallization could readily overprint the syn-eruptive crystallization history in mafic-intermediate systems. For instance, basaltic pumices from the Shishaldin volcano in Alaska show increasing crystallinity from rim to core due to post-fragmentation cooling in the atmosphere (Szramek et al., 2010).

Far-from-equilibrium crystallization is evident in plagioclase from

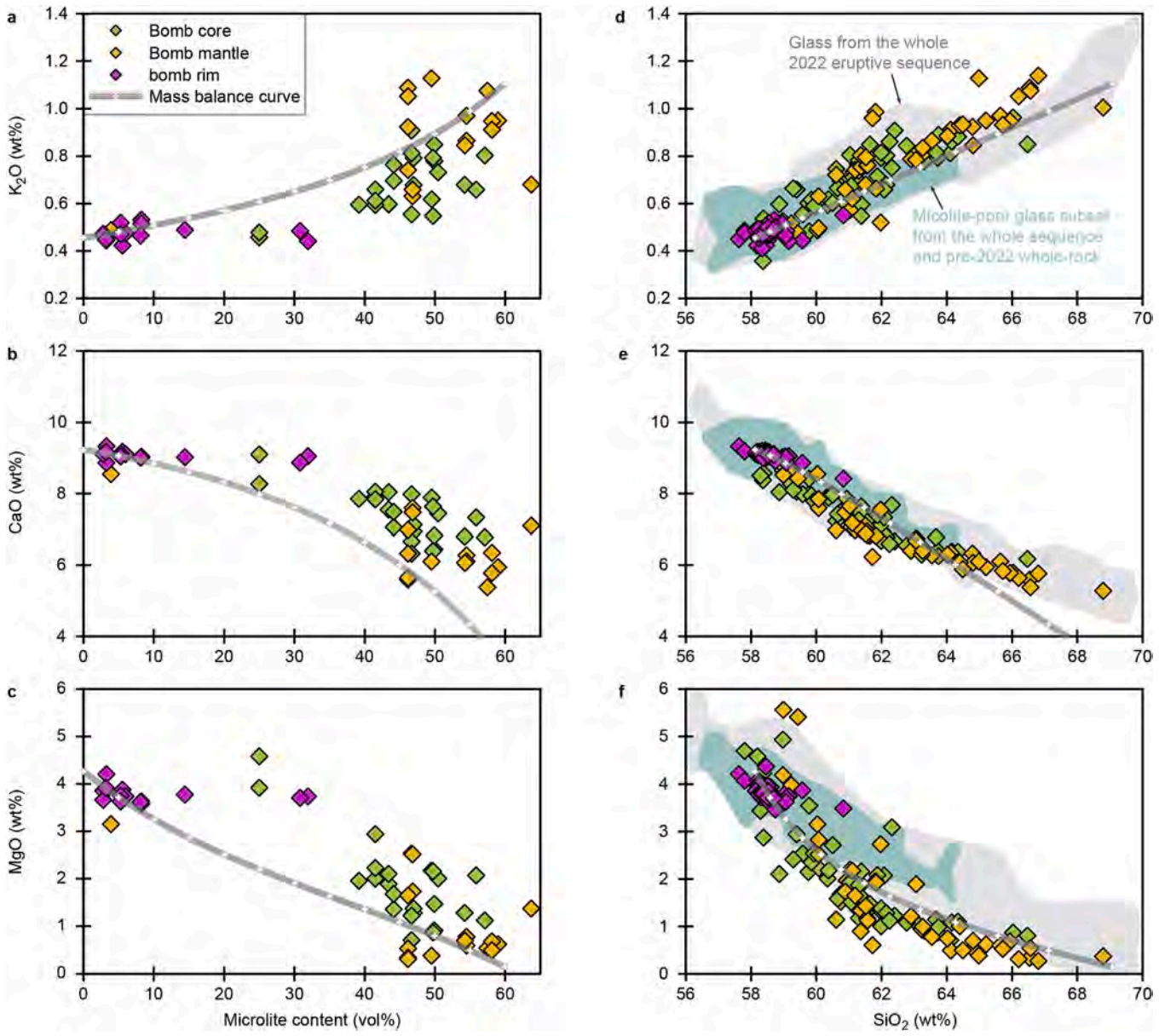

Fig. 5. Compositional variations in the 2022 Hunga bomb glass with changing microlite contents and SiO_2. (**a**) K_2O vs microlite content. (**b**) CaO vs microlite content. (**c**) MgO vs microite content. (**d**) K_2O vs SiO_2. (**e**) CaO vs SiO_2. (**f**) MgO vs SiO_2. Crosses in mass balance curves represent 5 vol% increase in microlite content.

the Hunga bomb, with microlites and phenocryst rims developing skeletal morphologies as well as becoming enriched in Si, Na, Fe, Mg, K and Ti and depleted in Al and Ca from the bomb rim to interior (Figs. 4b and S2). These crystals are always An#-poorer than phenocryst cores ($An_{67–82}$ vs $An_{83–95}$, Fig. 4a), consistent with melt evolution. Although clinopyroxene microlite crystallization rapidly depleted melt MgO (Fig. 5f), plagioclase rims and microlites show enrichment of Mg alongside other incompatible elements (e.g., Fe and Ti) if compared to phenocryst interiors (Figs. 4b and S2). This aligns with experimental results on increasing cooling rates affecting plagioclase-melt partitioning (Mollo et al., 2011). For instance, this can overrun An# effects on elemental partitioning (Bindeman and Davis, 2000; Mutch et al., 2022), as a more than two-fold MgO increase occurs with negligible An# decrease (<5 mol%; Fig. S2a), even with decreasing melt MgO (Fig. 5f). Accordingly, plagioclase composition reflects both melt composition and fast crystallization kinetics. Increasing compositional variability with decreasing An# (Figs. 4b and S2), may result from unrelaxed melt composition during rapid crystal growth.

Clinopyroxene rims and microlites become enriched in Al_2O_3 and TiO_2 with increasing CaO, opposite to phenocrystic interior, characterized by high CaO and low Al_2O_3 and TiO_2 (Fig. 4c). This correlates to increased Tschermak components at the expense of EnFs (Fig. S3c), reflecting fast, far-from-equilibrium crystal growth (Pontesilli et al., 2019). Increased Ca in rims and microlites coupled with decreased Mg# is seemingly at odds with the preferential incorporation of Mg over Fe^{2+} at both M1 and M2 sites at higher cooling rates (Mollo et al., 2010). This could be an effect of melt differentiation. However, clinopyroxene rims and microlites show almost an order of magnitude increase in Al_2O_3 (from 1.98 to 11.03 wt%) and TiO_2 (0.14 to 0.98 wt%) during crystallization, significantly larger than melt changes based on mass balance model (Al_2O_3 from 14.87 to 10.24 wt%, TiO_2 0.59 to 1.02 wt%, Table S5); calculations were performed by subtracting progressively increasing quantities of plagioclase and clinopyroxene microlites in proportions corresponding to those observed in the bomb, as microlites increase from 0 to 50 vol% (also see Appendix A for details of mass balance calculation). Diffusivities of Al and Ti in andesitic melt of D_{Al} =

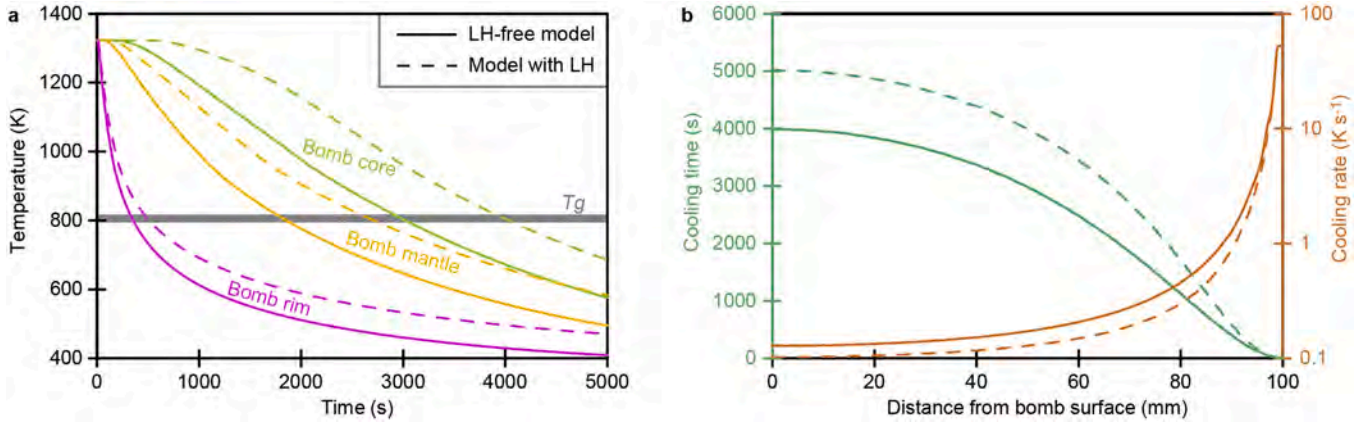

Fig. 6. Thermal modeling results for the 2022 Hunga bomb. (**a**) Temperature-time paths for the three portions of the bomb. (**b**) Cooling time between initial temperature and glass transition temperature (T_g) along with average cooling rate calculated on the same temperature interval across the whole bomb radius. Results are shown for both the latent heat (LH)-free model and the model considering the LH-effect.

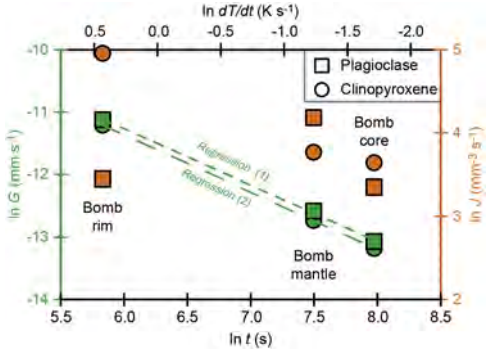

Fig. 7. Plots of crystal growth rate (*G*) and nucleation rate (*J*) against cooling time (*t*) and rate (*dT/dt*) for the 2022 Hunga bomb. The natural logarithms of all parameters estimated from CSD are plotted. Values are based on latent heat-free thermal model; results including the effect of latent heat are shown in figure S6. Growth rates are represented by green colored symbols, regression lines and axis, while the orange color is used for nucleation rates (symbols and axis). Linear regression (1) for plagioclase: $\ln G = -0.90\ln t - 5.87$ ($R^2 = 0.999$), $\ln G = 0.91\ln(dT/dt) - 11.48$ ($R^2 = 0.999$); linear regression (2) for clinopyroxene: $\ln G = -0.92\ln t - 5.87$ ($R^2 = 1$), $\ln G = 0.93\ln(dT/dt) - 11.59$ ($R^2 = 1$).

$0.035\ \mu m^2\ s^{-1}$ and $D_{Ti} = 0.212\ \mu m^2\ s^{-1}$ at $T = 1050\ ^\circ C$ (Zhang et al., 2010) imply that the total crystallization times ranging from 340 (bomb rim) to 3960 s (core), correspond to diffusive distances of 3–12 μm for Al and 8–29 μm for Ti. Therefore, slow diffusion of Al and Ti in silicate melts and fast cooling of the Hunga bomb determined diffusion-limited growth, causing far-from-equilibrium partitioning of Al and Ti in clinopyroxene.

Mineral-melt equilibrium criteria (Appendix A) suggest most clinopyroxene and all plagioclase mineral compositions from the bomb rim closely resemble equilibrium compositions with the surrounding melt, whereas crystals from the bomb interior largely reflect disequilibrium (Fig. 8), with their hypothetical equilibrium melt compositions being less evolved; e.g., higher measured An# than predicted and lower $K_D(Fe\text{-}Mg)^{cpx\text{-}melt}$ (= molar $(X_{Fe/Mg})^{clinopyroxene} / (X_{Fe/Mg})^{melt}$). Plagioclase from the bomb core, having the highest concentrations of incompatible Fe and Mg (Fig. 8a and b), also displays far-from-equilibrium An#. Similarly, clinopyroxene from the bomb rim having the lowest incompatible Al and Ti contents is in compositional equilibrium with the surrounding melt. Contrarily, a subgroup of clinopyroxene rims and microlites with the highest Al and Ti contents displays the largest ΔDiHd (i.e., Diopside-Hedenbergite) and $K_D(Fe\text{-}Mg)^{cpx\text{-}melt}$ (Fig. 8c and d). Compared to crystals from the bomb rim, stronger disequilibrium observed in those from the bomb interior seemingly contradicts their lower estimated cooling and crystallization rates (Fig. 7 and Table 1), although this is consistent with the increased proportion of skeletal and dendritic microlites and total microlite content; the closer-to-equilibrium feature at bomb rim is likely due to rapid quenching before further development of disequilibrium mineral textures. Hence, diffusional exchange was inhibited by the growing crystal network, promoting a transition from an interface- to a diffusion-limited growth regime (Kirkpatrick, 1975; Mollo and Hammer, 2017).

4.2. Melt evolution driven by microlite crystallization

The fresh 2022 Hunga bomb uniquely demonstrates the impact of late-stage groundmass crystallization on melt differentiation. A near-continuous transition from microlite-free glass at the bomb rim (Fig. 2a) to the largely crystalline (>50 vol%) core is observed (Fig. 2c). The increasingly crystalline groundmass shifts residual glass composition from andesitic to dacitic (58–69 wt% SiO_2), mimicking the entire glass compositional spectrum from the 2022 eruptive sequence (56–70 wt% SiO_2 with largely varying microlite contents, Fig. 5). Discarding syn/post-fragmentation melt modification by compiling a subset of microlite-poor glasses and pre-2022 whole-rock data, a much narrower compositional range is revealed (57–64 wt% SiO_2, Fig. 5; Brenna et al., 2022; Wu et al., 2026). Therefore, highly evolved glass compositions (SiO_2 >64%) at Hunga glass are linked to extensive microlite crystallization and should not be used to reconstruct pre-eruptive magmatic processes. Although this specific range applies to Hunga only, equivalent thresholds may be defined for other mafic to intermediate volcanic systems based on similar assessments of syn-eruptive and post-fragmentation processes, allowing for more accurate reconstructions of differentiation processes in magmatic reservoirs.

Glass from the bomb sample and microlite-poor glass from the 15 January 2022 eruption show similar major element melt evolution, except that the bomb glass becomes depleted in MgO (Fig. 5). This results from the crystallization of microlites in the bomb groundmass, whereas microlite-poor glass serves as a benchmark for groundmass glass differentiation related to phenocryst crystallization. The bomb glass MgO depletion thus likely stems from different mineral proportions and compositions between microlites and phenocrysts during far-from-equilibrium growth. Other mafic-intermediate volcanoes such as Tungurahua in Ecuador, also display large glass compositional variations when combining multiple bombs (Falasconi et al., 2023). However, the Hunga bomb uniquely provides a complete and continuous melt evolution history within a single pyroclast.

Most glass major elements (including K_2O, CaO, and MgO) show

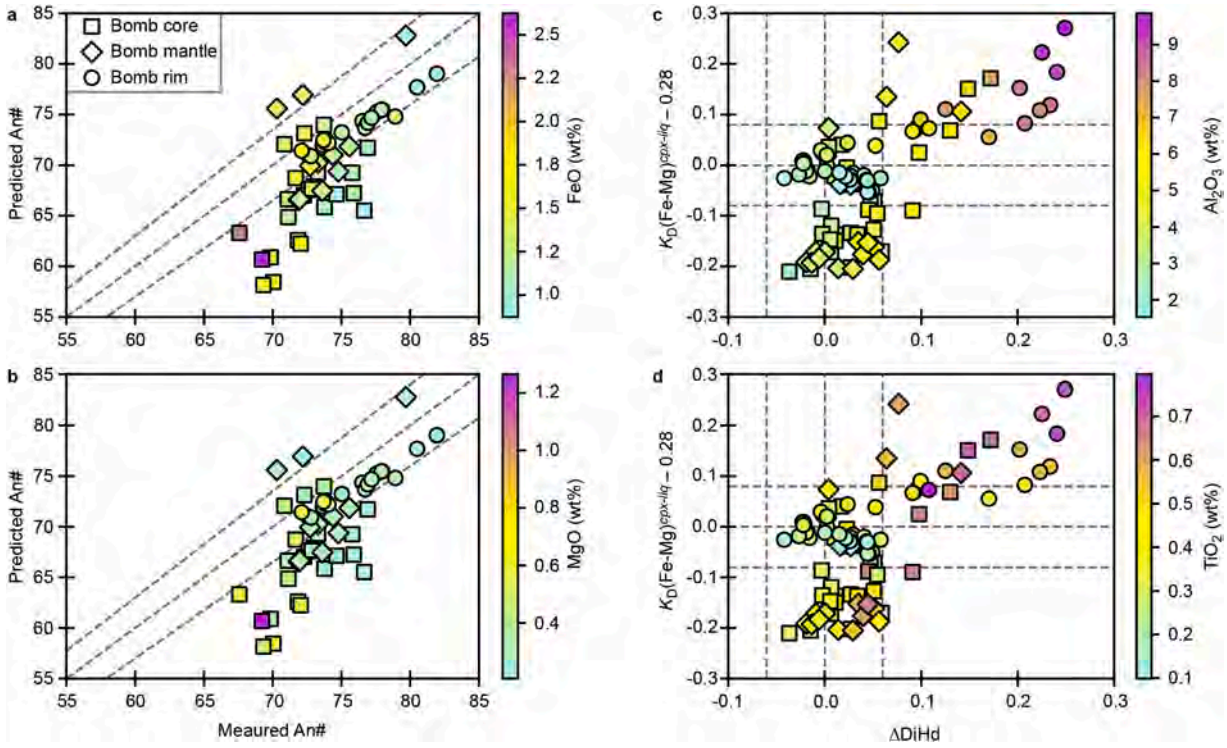

Fig. 8. Equilibrium test between rims and microlites and their hosting melts in the 2022 Hunga bomb. Markers are color-coded with mineral-incompatible element concentrations. (**a**) Predicted An# vs measured An# with FeO shown for plagioclase. (**b**) Predicted An# vs measured An# with MgO shown for plagioclase. (**c**) $K_D(Fe\text{-}Mg)^{cpx\text{-}liq}$ – 0.28 vs ΔDiHd with Al_2O_3 shown for clinopyroxene. (**d**) $K_D(Fe\text{-}Mg)^{cpx\text{-}liq}$ – 0.28 vs ΔDiHd with TiO_2 shown for clinopyroxene. The dashed lines show the equilibrium ranges when uncertainties are considered; ΔDiHd (i.e., Diopside-Hedenbergite) = ± 0.06, $K_D(Fe\text{-}Mg)^{cpx\text{-}melt}$ (= molar $(X_{Fe/Mg})^{clinopyroxene}$ / $(X_{Fe/Mg})^{melt}$) = 0.28 ± 0.08 for clinopyroxene and for plagioclase, and the upper and lower boundary lines represent 5% difference in predicted and measured An#.

limited variations at <10 vol% crystallinity but significant scatter at high crystallinity (>40 vol%) (Fig. 5a–c), confirming the post-fragmentation origin of microlites in the bomb. BSE imaging also reveals micron-scale glass compositional heterogeneities, visible as subtle grayscale variations in the residual glass (Fig. 2b and c), resulting from hindered diffusive relaxation of the interstitial melt within the growing crystal network. Mass balance calculations show that measured compositional variations lag behind predictions, especially at high crystallinity (Fig. 5a–c). For example, at 40–60 vol% microlites, only the most-evolved glass compositions align with mass balance results, while most others resemble compositions predicted at much lower crystallinity (lower K_2O and higher CaO and MgO; Fig. 5a–c), consistent with crystal growth under far-from-equilibrium conditions. However, excluding crystallinity, glass compositions generally follow mass balance predictions (Fig. 5d–f). Silica correlates positively with incompatible (e.g., K and P), and negatively with compatible (e.g., Ca and Mg) elements, consistent with mass balance at lower crystallinity (up to ~50 vol%; Figs. 5d–f and S4e). Accordingly, the Hunga bomb melt compositional evolution, driven by far-from-equilibrium crystallization of clinopyroxene and plagioclase microlites during post-fragmentation cooling, largely mimics near-equilibrium, pre-eruptive melt differentiation, mostly driven by the same mineral phases (Brenna et al., 2022). The main consequence is the divergence between observed and predicted microlite contents at similar glass/melt compositions, likely due to the inability for diffusion in the interstitial melt to keep pace with the fast crystallization kinetics at the higher microlite contents (Fig. 2b and c).

4.3. Reconstruction of the bomb thermal and solidification history

Integrating textural and compositional variations in the Hunga bomb with cooling timescales determined by thermal modeling provides a comprehensive view of post-fragmentation solidification processes. Numerical solutions of the heat equation (Eq. (7)) indicate a non-linear increase in the time required to reach the glass transition from the bomb surface to interior (Figs. 6b and S5), accompanied by a non-linear decrease in average cooling rate with increasing distance from the bomb surface, further accentuated when latent heat is considered (Fig. 6b). Notably, thermal models do not consider the development of fractures and the interaction with interconnected vesicles, although sporadic glassy regions suggest water permeation significantly affected local groundmass textures. Nevertheless, the observed textural gradient towards the bomb core is consistent with both the progressive decrease in estimated cooling rate and the non-linear variation in cooling trajectories. Indeed, bomb core and mantle textures are more similar to each other than to the rim (Figs. 2 and 6a).

Thermal models (with/without latent-heat) show cooling rates (from 0.1 K s^{-1} at the bomb core to 50 K s^{-1} at the bomb rim; Fig. 6) in the range for magma-water interaction (Fauria and Manga, 2018; Moitra et al., 2020), unlike cooling rates estimated for basaltic magma during ascent and emplacement as dikes or lava flows (0.0001–0.4 K s^{-1}; Cashman, 1993; Cashman et al., 1999; Di Fiore et al., 2021). In such cases, solidification of the largely degassed magmas favors plagioclase crystallization under high growth rates (Kirkpatrick, 1977). Conversely, cooling rates up to 50 K s^{-1} at the bomb rim pair with low plagioclase number density and nucleation rate (Figs. 3a and 7). Notably, plagioclase is typically absent in quenched basaltic-andesitic glasses (Cashman, 1993). In experiments, the suppression of plagioclase nucleation in mafic-intermediate magmas is attributed to high cooling rates (or degrees of undercooling; Waters et al., 2015; Le Gall et al., 2021), consistent with the nucleation theory of Kirkpatrick (1983). In this theory, nucleation and growth rates are controlled by the addition of cation-centered tetrahedral units, where the activation energy is proportional to the number of bonds between tetrahedrally coordinated cations and surrounding oxygen anions. Hence, the less polymerized

crystalline phases will nucleate preferentially (Kirkpatrick, 1983). This reconciles with higher nucleation rates for clinopyroxene, consistent with decompression/cooling experiments (Pupier et al., 2008; Brugger and Hammer, 2010; Arzilli et al., 2015; Pontesilli et al., 2019; Le Gall et al., 2021).

The heterogeneous microlite morphologies in the Hunga bomb (Fig. 2) align with rapid cooling as well as high growth rates estimated for clinopyroxene and plagioclase (Table 1). Textural features and growth rates resemble disequilibrium experiments, showing fast, diffusion-limited crystallization at high degrees of undercooling (Ni et al., 2014; Arzilli et al., 2015; Pontesilli et al., 2019; Le Gall et al., 2021; Arzilli et al., 2022; Welsch et al., 2023). Noteworthy is the increasing occurrence of skeletal and dendritic morphologies, along with increased microlite-melt chemical disequilibrium, towards the bomb interior, seemingly at odds with the highest cooling rates estimated for the bomb rim, where instead the less developed crystal populations show compositional and textural features expected to develop at close to equilibrium conditions. Indeed, in-situ observations show that often complex crystal morphologies develop later in time, as faceted olivine crystals develop hopper-shaped protrusions in single-step undercooling (Ni et al., 2014) and dendritic branches depart from euhedral clinopyroxene crystals with increasing undercooling (Arzilli et al., 2022). In cooling and/or decompressing/degassing magmas, increasing crystallinity and melt evolution limit the mobility of chemical species at growing crystal-melt interfaces by affecting chemical diffusivity and diffusion pathways inside crystal networks, promoting diffusion-limited growth and the development of morphologically complex crystals (Kirkpatrick, 1977; Mollo and Hammer, 2017; Pontesilli et al., 2019), consistent with the observed increasing degree of chemical disequilibrium (Fig. 8). The shift from interface- to diffusion-limited growth regimes, is accompanied by the formation of skeletal/dendritic crystal morphologies and by almost an order of magnitude increase in crystal growth rates (Arzilli et al., 2022). Accordingly, crystallization kinetics determined in rapidly cooled rocks and in disequilibrium experiments may only represent minimum rates for crystal growth, as the assumptions of crystallization as a continuous and steady process may hold true only for faceted crystals growing at low undercooling regimes (Le Gall et al., 2021; Arzilli et al., 2022; Welsch et al., 2023).

Growth rates based on CSD calculations inversely correlate with crystallization time in logarithmic plots, mirroring a direct correlation with cooling rate (Fig. 7). Static, ambient-pressure experiments (Pupier et al., 2008) show that higher cooling rates (and undercooling) favor nucleation over growth, steepening plagioclase CSD slopes. In the Hunga bomb, mostly parallel plagioclase and clinopyroxene CSDs (Fig. 3c and d), indicate overall similar roles of nucleation and growth across the bomb (Marsh, 1988, 1998) (except for plagioclase at the bomb rim, Fig. 7). The small Avrami numbers (Av, <1; Table 1) suggest that over the investigated range of cooling rates, crystallization kinetics, not heat loss, controlled the development of crystallinity and thus the final groundmass texture (see details in Appendix A; Hort and Spohn, 1991). Therefore, increasing heat loss essentially determined the decrease in crystallization time (T_i to T_g) from the bomb core to the rim. The shift of CSD curves toward higher number density and increased crystal abundance from rim to core (Fig. 3) likely reflect the overall longer timescale for crystal growth (Marsh, 1988).

Traditionally, constant negative CSD slopes in closed systems (such as rapidly cooling tephra) imply exponentially increasing nucleation rates over time (assuming constant or inversely time-related growth; Marsh, 1988, 1998). While some natural systems may experience increasing undercooling and nucleation (e.g., degassing and accelerating magma in volcanic conduits; Martel and Schmidt, 2003), cooling intrusions and lava flows experience decreasing cooling rates following emplacement, due to latent heat of crystallization and insulation (Cashman et al., 1999; Di Fiore et al., 2023). Despite the linear CSD slopes in the Hunga bomb (Fig. 3), its thermal history is inconsistent with exponentially increasing nucleation with time. This is clear, considering that different sites within the bomb experienced different cooling histories, and yet, show apparently similar nucleation rates. More generally, an exponential increase in nucleation rate with time is inconsistent with nucleation occurring typically over a short period of time after initial system perturbation causing high undercooling/supersaturation. Moreover, non-constant crystal growth rates rule out simple growth-nucleation rate correlations causing linear CSD trends if all crystals grew at the same rate (Eberl et al., 1998).

The negative CSD slopes in the bomb may then arise from size-dependent growth, whereby larger crystals grow faster (Marsh, 1998). Increasing morphologically complex crystals with disequilibrium compositions towards the bomb interior (Figs. 2 and 8) align with non-linear crystal growth, where initially euhedral crystals may experience an acceleration in the instantaneous growth rate while developing more complex morphologies (Ni et al., 2014; Arzilli et al., 2022; Welsch et al., 2023). Impurities incorporated during growth and stress-induced lattice dislocations are proportional to crystal size, and facilitate surface attachment kinetics (Garside and Davey, 1980). Moreover, small crystals near the critical radius may grow extremely slow due to the Gibbs-Thomson effect (Mullin, 2001). These factors suggest microlite crystallization likely proceeds via size-dependent growth and growth rate dispersion, as smaller particles grow into larger sizes in response to Brownian motion-driven attachment of chemical constituents, with the result that progressively fewer crystals will grow into larger size classes (Eberl et al., 1998, 2002). Crystal populations grown in this way will necessarily show growth rate peaks exceeding constant growth expectations (e.g., Arzilli et al., 2022; Welsch et al., 2023). Accordingly, observed CSD trends in natural, closed systems may reflect unsteady, size-dependent and dispersive crystallization kinetics. Applying constant growth rates to rapidly cooled magma bodies syn/post-intrusion/eruption requires caution to avoid biased timescale estimations.

5. Conclusions and implications

Our findings indicate that standard tools to reconstruct magma evolution and dynamics driving hazardous scenarios, such as one of the largest eruptions in historical times at Hunga, may be misdirected by processes occurring during syn- to post-fragmentation crystallization. Examination of a submarine-cooled bomb reveals a gradual increase in crystallinity from the microlite-free bomb rim to the highly crystallized interior, encompassing a wider range of crystallinity than typically found in individual pyroclasts of smaller grain size. Such cooling-induced gradual growth of plagioclase and clinopyroxene microlites results in large compositional variations in groundmass glass, allowing a more direct comparison with closed-system experimental scenarios. However, mass balance suggests a delayed melt compositional change, due to diffusional chemical exchange reducing once crystallization becomes too rapid and melt pockets becoming isolated by the crystal network. Regardless of this delay in melt evolution, major elements are consistent with mass balance calculations involving the mineral phases forming in the magma reservoir. Therefore, glass major element evolutionary trends cannot be easily distinguished from pre-eruptive fractional crystallization in the magma reservoir, possibly resulting from overall similar microlite and phenocryst assemblages. Microlite crystallization in this single bomb produced melt compositions spanning the whole 2022 Hunga compositional range. This shows how melt evolution is more sensitive to the overall mineral assemblage and proportions, and hence mass balance alone may not be enough to distinguish between close-to-equilibrium storage processes and fast-paced, syn- to post-eruptive crystallization scenarios.

This work highlights that a careful analysis of rock textures should precede any study using pyroclasts to reconstruct magma chamber processes. Particularly, evidence of rapid and especially far-from-equilibrium crystallization, such as extreme length-width ratios of

crystal phases and wide diversity in microlite contents in a rock suite should be warning signs. Interpreting such rock samples may lead to false evolution scenarios. Microlite growth may result in zoned residual glasses as chemical diffusion may be slower than fast-paced groundmass crystallization (Mollo and Hammer, 2017; Pontesilli et al., 2019). Moreover, the crystallization of disequilibrium mineral compositions may have a disproportionate effect on residual glass compositions (Mollo et al., 2011; McCarthy et al., 2023). If these conditions exist in a pyroclastic suite, whole-rock compositional methods may be more reliable for examining magma reservoir processes. The delayed melt evolution with increasing microlites during rapid growth in the Hunga bomb, evidenced by unrelaxed glass boundary layers, suggests that pyroclastic samples with <10 vol% microlites are largely unaffected by post-fragmentation crystallization. This threshold represents a safety guide for identifying representative pre-eruptive melt compositions in mafic-intermediate systems, as well as for accurate distal tephra correlation.

Thermal models show that the temporal window for crystallization increases significantly from the glassy rim of the bomb to its core, mirroring the observed crystallinity gradient. These timescales enable an independent assessment of crystallization kinetics based on the observed incremental textural development, revealing extremely rapid crystallization due to magma cooling in seawater, even though such swift kinetics represent only minima. On the other hand, estimated cooling timescales, calculated over the entire temperature interval between eruption and glass transition, represent maxima. Consistent with recent experimental findings, textural analyses and crystal-melt equilibrium modeling provide compelling natural evidence that unsteady (time-dependent) and dispersive (size-dependent) crystallization kinetics characterize rapidly-cooling magma, as in syn- and post-eruption scenarios. This emphasizes caution when applying steady-state, lab-derived growth rates to reconstruct the timescales of natural, far-from-equilibrium processes from crystal size distributions. For instance, the slope of crystal size distributions may depend more on size-dependent growth than the crystallization timescale itself (Eberl et al., 2002), possibly leading to severe over- or under- estimations of magmatic timescales when simplistic assumptions are made. During complex magmatic processes simple kinetics-time relations are easily over-simplified (e.g., Marsh, 1998), while textural modeling based on thermodynamics and kinetics laws is still a challenge.

This zoned bomb provided a natural laboratory that allowed demonstration of how differential development of crystal textures, compositions led to widely diverse interstitial glass evolution that if taken out of context could skew understanding of pre-eruptive magmatic processes. Our results underscore the importance of integrating careful microanalytical work with independent constraints such as numerical models, in active volcanic areas to ensure meaningful interpretation of compositional and textural variations in eruptive products.

CRediT authorship contribution statement

Jie Wu: Writing – review & editing, Writing – original draft, Visualization, Validation, Methodology, Investigation, Formal analysis, Data curation, Conceptualization. **Alessio Pontesilli:** Writing – review & editing, Writing – original draft, Visualization, Validation, Methodology, Investigation, Formal analysis, Data curation, Conceptualization. **Marco Brenna:** Writing – review & editing, Writing – original draft, Supervision, Project administration, Methodology, Funding acquisition, Formal analysis. **Shane J. Cronin:** Writing – review & editing, Writing – original draft, Supervision, Project administration, Methodology, Investigation, Funding acquisition, Formal analysis, Data curation, Conceptualization. **Sung-Hyun Park:** Writing – review & editing, Resources, Funding acquisition. **Joali Paredes-Mariño:** Writing – review & editing, Data curation. **Kyle Hamilton:** Writing – review & editing, Data curation. **Marta Ribó:** Writing – review & editing. **David Adams:** Writing – review & editing, Data curation. **Mila Huebsch:** Writing – review & editing.

Declaration of competing interest

Authors declare that they have no competing interests.

Acknowledgments

We thank the Captain and Crew of RV Aaron, on the K-HEART voyage during April 2022. The sampling of the bomb was supported by the Korea Polar Research Institute (KOPRI) under project PE225500 and KOPRI kindly allowed S.J.C. to visit and subsample this in Incheon. Fabrizio Di Fiore and Alex Scarani are acknowledged for the insightful discussions on thermal modeling. We thank Editor Rosemary Hickey-Vargas for editorial handling, and Martin Mangler and an anonymous reviewer for constructive comments and suggestions. This work was supported by Royal Society of New Zealand Te Apārangi Marsden Fund (MFP-UOO2218), New Zealand Government Ministry of Business Innovation and Employment Endeavour Research Program (UOAX1913, UOA24103), Ministero dell'Università e della Ricerca - MUR-PNRR (NGEU) IR0000025 Project (D53C22001400005), and Korea Polar Research Institute (PE22550).

Supplementary materials

Supplementary material associated with this article can be found, in the online version, at doi:10.1016/j.epsl.2026.120052.

Data availability

All data are available in the main text or the supplementary materials.

References

Armienti, P., 2008. Decryption of igneous rock textures: crystal size distribution tools. Rev. Mineral. Geochem. 69, 623–649. https://doi.org/10.2138/rmg.2008.69.16.

Arzilli, F., Agostini, C., Landi, P., Fortunati, A., Mancini, L., Carroll, M.R., 2015. Plagioclase nucleation and growth kinetics in a hydrous basaltic melt by decompression experiments. Contrib. Mineral. Petrol. 170, 55. https://doi.org/10.1007/s00410-015-1205-9.

Arzilli, F., Polacci, M., La Spina, G., Le Gall, N., Llewellin, E.W., Brooker, R.A., Torres-Orozco, R., Di Genova, D., Neave, D.A., Hartley, M.E., Mader, H.M., Giordano, D., Atwood, R., Lee, P.D., Heidelbach, F., Burton, M.R., 2022. Dendritic crystallization in hydrous basaltic magmas controls magma mobility within the Earth's crust. Nat. Commun. 13, 3354. https://doi.org/10.1038/s41467-022-30890-8.

Ball, M., Pinkerton, H., 2006. Factors affecting the accuracy of thermal imaging cameras in volcanology. J. Geophys. Res.-Solid Earth 111. https://doi.org/10.1029/2005JB003829.

Bergman, T.L., 2011. Fundamentals of Heat and Mass Transfer. Wiley.

Bindeman, I.N., Davis, A.M., 2000. Trace element partitioning between plagioclase and melt: investigation of dopant influence on partition behavior. Geochim. Cosmochim. Acta 64, 2863–2878. https://doi.org/10.1016/S0016-7037(00)00389-6.

Borrero, J.C., Cronin, S.J., Latu'ila, F.H., Tukuafu, P., Heni, N., Tupou, A.M., Kula, T., Fa'anunu, O., Bosserelle, C., Lane, E., 2023. Tsunami runup and inundation in Tonga from the January 2022 eruption of Hunga Volcano. Pure Appl. Geophys. 180, 1–22. https://doi.org/10.1007/s00024-022-03215-5.

Brenna, M., Cronin, S.J., Smith, I.E., Pontesilli, A., Tost, M., Barker, S., Tonga'onevai, S., Kula, T., Vaiomounga, R., 2022. Post-caldera volcanism reveals shallow priming of an intra-ocean arc andesitic caldera: hunga volcano, Tonga, SW Pacific. Lithos. 412, 106614. https://doi.org/10.1016/j.lithos.2022.106614.

Brugger, C.R., Hammer, J.E., 2010. Crystal size distribution analysis of plagioclase in experimentally decompressed hydrous rhyodacite magma. Earth Planet. Sci. Lett. 300, 246–254. https://doi.org/10.1016/j.epsl.2010.09.046.

Cashman, K.V., 1992. Groundmass crystallization of Mount St. Helens dacite, 1980–1986: a tool for interpreting shallow magmatic processes. Contrib. Mineral. Petrol. 109, 431–449. https://doi.org/10.1007/BF00306547.

Cashman, K.V., 1993. Relationship between plagioclase crystallization and cooling rate in basaltic melts. Contrib. Mineral. Petrol. 113, 126–142. https://doi.org/10.1007/BF00320836.

Cashman, K.V., 2020. Crystal size distribution (CSD) analysis of volcanic samples: advances and challenges. Front. Earth Sci. 8, 291. https://doi.org/10.3389/feart.2020.00291.

Cashman, K.V., Thornber, C., Kauahikaua, J.P., 1999. Cooling and crystallization of lava in open channels, and the transition of Pāhoehoe Lava to'A'ā. Bull. Volcanol. 61, 306–323. https://doi.org/10.1007/s004450050299.
Chistyakova, S., Latypov, R., 2010. On the development of internal chemical zonation in small mafic dykes. Geol. Mag. 147, 1–12. https://doi.org/10.1017/S0016756809990343.
Clare, M.A., Yeo, I.A., Watson, S., Wysoczanski, R., Seabrook, S., Mackay, K., Hunt, J.E., Lane, E., Talling, P.J., Pope, E., 2023. Fast and destructive density currents created by ocean-entering volcanic eruptions. Science 381, 1085–1092. https://www.science.org/doi/10.1126/science.adi3038.
Colombier, M., Scheu, B., Wadsworth, F.B., Cronin, S., Vasseur, J., Dobson, K.J., Hess, K. U., Tost, M., Yilmaz, T., Cimarelli, C., 2018. Vesiculation and quenching during surtseyan eruptions at hunga tonga-hunga ha'apai volcano, tonga. J. Geophys. Res.-Solid Earth 123, 3762–3779. https://doi.org/10.1029/2017JB015357.
Cronin, S., Brenna, M., Smith, I., Barker, S., Tost, M., Ford, M., Tonga'onevai, S., Kula, T., Vaiomounga, R., 2017. New volcanic island unveils explosive past. Eos. (Washington. DC) 98, 1. https://doi.org/10.1029/2017EO076589.
Di Fiore, F., Mollo, S., Vona, A., MacDonald, A., Ubide, T., Nazzari, M., Romano, C., Scarlato, P., 2021. Kinetic partitioning of major and trace cations between clinopyroxene and phonotephritic melt under convective stirring conditions: new insights into clinopyroxene sector zoning and concentric zoning. Chem. Geol. 584, 120531. https://doi.org/10.1016/j.chemgeo.2021.120531.
Di Fiore, F., Vona, A., Scarani, A., Giordano, G., Romano, C., Giordano, D., Caricchi, L., Martin Lorenzo, A., Rodriguez, F., Coldwell, B., 2023. Experimental constraints on the rheology of lavas from 2021 Cumbre Vieja eruption (La Palma, Spain). Geophys. Res. Lett. 50, e2022GL100970. https://doi.org/10.1029/2022GL100970.
Eberl, D., Drits, V., Srodon, J., 1998. Deducing growth mechanisms for minerals from the shapes of crystal size distributions. Am. J. Sci. 298, 499–533. https://doi.org/10.2475/ajs.298.6.499.
Eberl, D., Kile, D.E., Drits, V., 2002. On geological interpretations of crystal size distributions: constant vs. proportionate growth. Am. Miner. 87, 1235–1241. https://doi.org/10.2138/am-2002-8-923.
Falasconi, A., Cioni, R., Bernard, B., Samaniego, P., Pistolesi, M., Schiavi, F., 2023. What controls the formation of vulcanian bombs? A case study from the 1 February 2014 eruption of Tungurahua (Ecuador). J. Volcanol. Geotherm. Res. 444, 107961. https://doi.org/10.1016/j.jvolgeores.2023.107961.
Fauria, K.E., Manga, M., 2018. Pyroclast cooling and saturation in water. J. Volcanol. Geotherm. Res. 362, 17–31. https://doi.org/10.1016/j.jvolgeores.2018.07.002.
Garside, J., Davey, R.J., 1980. Invited review secondary contact nucleation: kinetics, growth and scale-up. Chem. Eng. Commun. 4, 393–424. https://doi.org/10.1080/00986448008935918.
Gupta, A.K., Bennartz, R., Fauria, K.E., Mittal, T., 2022. Eruption chronology of the December 2021 to January 2022 Hunga Tonga-Hunga Ha'apai eruption sequence. Commun. Earth Environ. 3, 314. https://doi.org/10.1038/s43247-022-00606-3.
Hafsteinsdóttir, A.K., 2024. The Effect of Microlite Crystallization on Melt Compositions and Derived Magma Temperatures in the 2021 and 2022 Fagradalsfjall Eruptions. University of Iceland. PhD thesis. https://hdl.handle.net/1946/46273.
Hammer, J.E., Cashman, K.V., Hoblitt, R.P., Newman, S., 1999. Degassing and microlite crystallization during pre-climactic events of the 1991 eruption of Mt. Pinatubo, Philippines. Bull. Volcanol. 60, 355–380. https://doi.org/10.1007/s004450050238.
Hammer, J.E., Rutherford, M.J., 2002. An experimental study of the kinetics of decompression-induced crystallization in silicic melt. J. Geophys. Res.-Solid Earth 107. https://doi.org/10.1029/2001JB000281. ECV 8-1-ECV 8-24.
Higgins, M.D., 2000. Measurement of crystal size distributions. Am. Miner. 85, 1105–1116. https://doi.org/10.2138/am-2000-8-901.
Hofmeister, A.M., Sehlke, A., Avard, G., Bollasina, A.J., Robert, G., Whittington, A.G., 2016. Transport properties of glassy and molten lavas as a function of temperature and composition. J. Volcanol. Geotherm. Res. 327, 330–348. https://doi.org/10.1016/j.jvolgeores.2016.08.015.
Hort, M., Spohn, T., 1991. Crystallization calculations for a binary melt cooling at constant rates of heat removal: implications for the crystallization of magma bodies. Earth Planet. Sci. Lett. 107, 463–474. https://doi.org/10.1016/0012-821X(91)90093-W.
Hunt, J.B., Hill, P.G., 1993. Tephra geochemistry: a discussion of some persistent analytical problems. Holocene 3, 271–278. https://doi.org/10.1177/095968369300300310.
Hutchison, W., Sugden, P., Burke, A., Abbott, P., Ponomareva, V.V., Dirksen, O., Portnyagin, M.V., MacInnes, B., Bourgeois, J., Fitzhugh, B., 2025. The 1831 CE mystery eruption identified as Zavaritskii caldera, Simushir Island (Kurils). Proc. Natl. Acad. Sci 122, e2416699122. https://doi.org/10.1073/pnas.2416699122.
Kirkpatrick, R.J., 1975. Crystal growth from the melt: a review. Am. Miner. 60, 798–814.
Kirkpatrick, R.J., 1977. Nucleation and growth of plagioclase, Makaopuhi and Alae lava lakes, Kilauea Volcano, Hawaii. Geol. Soc. Am. Bull. 88, 78–84. https://doi.org/10.1130/0016-7606(1977)88<78:NAGOPM>2.0.CO;2.
Kirkpatrick, R.J., 1983. Theory of nucleation in silicate melts. Am. Miner. 68, 66–77.
Langhammer, D., Di Genova, D., Steinle-Neumann, G., 2022. Modeling viscosity of volcanic melts with artificial neural networks. Geochem. Geophys. Geosyst. 23, e2022GC010673. https://doi.org/10.1029/2022GC010673.
Le Gall, N., Arzilli, F., La Spina, G., Polacci, M., Cai, B., Hartley, M.E., Vo, N.T., Atwood, R.C., Di Genova, D., Nonni, S., Llewellin, E.W., Burton, M.R., Lee, P.D., 2021. In situ quantification of crystallisation kinetics of plagioclase and clinopyroxene in basaltic magma: implications for lava flow. Earth Planet. Sci. Lett. 568, 117016. https://doi.org/10.1016/j.epsl.2021.117016.
Le Mével, H., Miller, C.A., Ribó, M., Cronin, S., Kula, T., 2023. The magmatic system under Hunga volcano before and after the 15 January 2022 eruption. Sci. Adv. 9, eadh3156. https://science.org/doi/full/10.1126/sciadv.adh3156.
Lide, D.R., 2004. CRC Handbook of Chemistry and Physics. CRC.
Lormand, C., Zellmer, G.F., Kilgour, G.N., Németh, K., Palmer, A.S., Sakamoto, N., Yurimoto, H., Kuritani, T., Iizuka, Y., Moebis, A., 2020. Slow ascent of unusually hot intermediate magmas triggering Strombolian to sub-Plinian eruptions. J. Petrol. 61, egaa077. https://doi.org/10.1093/petrology/egaa077.
Mangler, M.F., Humphreys, M.C., Wadsworth, F.B., Iveson, A.A., Higgins, M.D., 2022. Variation of plagioclase shape with size in intermediate magmas: a window into incipient plagioclase crystallisation. Contrib. Mineral. Petrol. 177, 64. https://doi.org/10.1007/s00410-022-01922-9.
Marsh, B.D., 1988. Crystal size distribution (CSD) in rocks and the kinetics and dynamics of crystallization. Contrib. Mineral. Petrol. 99, 277–291. https://doi.org/10.1007/BF00375362.
Marsh, B.D., 1998. On the interpretation of crystal size distributions in magmatic systems. J. Petrol. 39, 553–599. https://doi.org/10.1093/petroj/39.4.553.
Martel, C., Schmidt, B.C., 2003. Decompression experiments as an insight into ascent rates of silicic magmas. Contrib. Mineral. Petrol. 144, 397–415. https://doi.org/10.1007/s00410-002-0404-3.
McCarthy, A., Chelle-Michou, C., Blundy, J.D., Dorais, M.J., Van der Zwan, F.M., Peate, D.W., 2023. The effect of variations in cooling rates on mineral compositions in mid-ocean ridge basalts. Chem. Geol. 625, 121415. https://doi.org/10.1016/j.chemgeo.2023.121415.
Moitra, P., Sonder, I., Valentine, G.A., 2018. Effects of size and temperature-dependent thermal conductivity on the cooling of pyroclasts in air. Geochem. Geophys. Geosyst. 19, 3623–3636. https://doi.org/10.1029/2018GC007510.
Moitra, P., Sonder, I., Valentine, G.A., 2020. The role of external water on rapid cooling and fragmentation of magma. Earth Planet. Sci. Lett. 537, 116194. https://doi.org/10.1016/j.epsl.2020.116194.
Mollo, S., Del Gaudio, P., Ventura, G., Iezzi, G., Scarlato, P., 2010. Dependence of clinopyroxene composition on cooling rate in basaltic magmas: implications for thermobarometry. Lithos. 118, 302–312. https://doi.org/10.1016/j.lithos.2010.05.006.
Mollo, S., Hammer, J.E., 2017. Dynamic crystallization in magmas. Eur. Mineral. Union Notes Mineral. 16, 373–418. https://doi.org/10.1180/EMU-notes.16.12.
Mollo, S., Putirka, K., Iezzi, G., Del Gaudio, P., Scarlato, P., 2011. Plagioclase–melt (dis) equilibrium due to cooling dynamics: implications for thermometry, barometry and hygrometry. Lithos. 125, 221–235. https://doi.org/10.1016/j.lithos.2011.02.008.
Mullin, J., 2001. Crystallization. Butterworth-Heinemann.
Mutch, E.J., Maclennan, J., Madden-Nadeau, A.L., 2022. The dichotomous nature of Mg partitioning between plagioclase and melt: implications for diffusion chronometry. Geochim. Cosmochim. Acta 339, 173–189. https://doi.org/10.1016/j.gca.2022.10.035.
Ni, H., Keppler, H., Walte, N., Schiavi, F., Chen, Y., Masotta, M., Li, Z., 2014. In situ observation of crystal growth in a basalt melt and the development of crystal size distribution in igneous rocks. Contrib. Mineral. Petrol. 167, 1003. https://doi.org/10.1007/s00410-014-1003-9.
Petrone, C.M., Mollo, S., Gertisser, R., Buret, Y., Scarlato, P., Del Bello, E., Andronico, D., Ellis, B., Pontesilli, A., De Astis, G., 2022. Magma recharge and mush rejuvenation drive paroxysmal activity at Stromboli volcano. Nat. Commun. 13, 7717. https://doi.org/10.1038/s41467-022-35405-z.
Pontesilli, A., Masotta, M., Nazzari, M., Mollo, S., Armienti, P., Scarlato, P., Brenna, M., 2019. Crystallization kinetics of clinopyroxene and titanomagnetite growing from a trachybasaltic melt: new insights from isothermal time-series experiments. Chem. Geol. 510, 113–129. https://doi.org/10.1016/j.chemgeo.2019.02.015.
Proud, S.R., Prata, A.T., Schmauß, S., 2022. The January 2022 eruption of Hunga Tonga-Hunga Ha'apai volcano reached the mesosphere. Science 378, 554–557. https://science.org/doi/abs/10.1126/science.abo4076.
Pupier, E., Duchene, S., Toplis, M.J., 2008. Experimental quantification of plagioclase crystal size distribution during cooling of a basaltic liquid. Contrib. Mineral. Petrol. 155, 555–570. https://doi.org/10.1007/s00410-007-0258-9.
Putirka, K.D., 2008. Thermometers and barometers for volcanic systems. Rev. Mineral. Geochem. 69, 61–120. https://doi.org/10.2138/rmg.2008.69.3.
Randolph, A.D., Larson, M.A., 1988. Theory of Particulate Processes: Analysis and Techniques of Continuous Crystallization. Elsevier.
Ribo, M., Cronin, S., Stern, S., Park, S.-H., Garvin, J., Kula, T., 2023. Morphological evolution of the Hunga Tonga-Hunga Ha'apai submarine volcano after the explosive eruption. In: EGU General Assembly Conference Abstracts. Vienna. https://doi.org/10.5194/egusphere-egu23-17221.
Saltykov, S., 1949. Calculation of the distribution curves for the size of dispersed grains. Plant Lab. 15, 1317–1319.
Schwartz, H., 1939. Metallographic determination of the size distribution of tempered carbon nodules. Met. Alloy. 5, 139–140.
Skeel, R.D., Berzins, M., 1990. A method for the spatial discretization of parabolic equations in one space variable. SIAM J. Sci. Comput. 11, 1–32. https://doi.org/10.1137/0911001.
Stebbins, J., Carmichael, I., Moret, L., 1984. Heat capacities and entropies of silicate liquids and glasses. Contrib. Mineral. Petrol. 86, 131–148. https://doi.org/10.1007/BF00381840.
Szramek, L., Gardner, J.E., Hort, M., 2010. Cooling-induced crystallization of microlite crystals in two basaltic pumice clasts. Am. Miner. 95, 503–509. https://doi.org/10.2138/am.2010.3270.
Waters, L.E., Andrews, B.J., Lange, R.A., 2015. Rapid crystallization of plagioclase phenocrysts in silicic melts during fluid-saturated ascent: phase equilibrium and decompression experiments. J. Petrol. 56, 981–1006. https://doi.org/10.1093/petrology/egv025.

Welsch, B., Faure, F., First, E.C., 2023. Reappraising crystallization kinetics with overgrowth chronometry: an in situ study of olivine growth velocities. J. Petrol. 64. https://doi.org/10.1093/petrology/egad055.

Wu, J., Cronin, S.J., Brenna, M., Park, S.-H., Pontesilli, A., Ukstins, I.A., Adams, D., Paredes-Mariño, J., Hamilton, K., Huebsch, M., González-García, D., Firth, C., White, J.D.L., Nichols, A.R.L., Plank, T., Vongsvivut, J., Klein, A., Ramos, F., Latu'ila, F., Kula, T., 2025. Low sulfur emissions from 2022 Hunga eruption due to seawater-magma interactions. Nat. Geosci. 18, 518–524. https://doi.org/10.1038/s41561-025-01691-7.

Wu, J., Cronin, S.J., Brenna, M., Paredes-Mariño, J., Park, S.H., Huebsch, M., Pontesilli, A., Firth, C., Adams, D., Ubide, T., Hamilton, K., MacDonald, A., Califano, E., White, J.D.L., Plank, T., Ribó, M., Ukstins, I., Ramos, F., Mollo, S., Kim, J., Latu'ila, F., Kula, T., Vaiomounga, R., 2026. What triggered the catastrophic 15 January 2022 Hunga eruption? Earth Planet. Sci. Lett. https://doi.org/10.1016/j.epsl.2026.120041.

Zhang, Y., Ni, H., Chen, Y., 2010. Diffusion data in silicate melts. Rev. Mineral. Geochem. 72, 311–408. https://doi.org/10.2138/rmg.2010.72.8.